arXiv:1404.5136v1 [cond-mat.soft] 21 Apr 2014

Effects of interfaces on dynamics in micro-fluidic devices: slip-boundaries' impact on rotation characteristics of polar liquid film motors

Zhong-Qiang Liu[1],* Su-Rong Jiang[1], Tamar A. Yinnon[2], Xiang-Mu Kong[1], and Ying-Jun Li[3]

[1]*Department of Physics, Qufu Normal University, Qufu 273165, China*

[2]*K. Kalia, D.N. Kikar, Jordan 90666, Israel*

[3]*SMCE, China University of Mining and Technology, Beijing 100083, China*

(Dated: April 22, 2014)

Abstract

Slip-boundary effects on the polar liquid film motor (PLFM) – a novel micro-fluidic device with important implications for advancing knowledge on liquid micro-film's structure, dynamics, modeling and technology – are studied. We develop a mathematical model, under slip boundary conditions, describing electro-hydro-dynamical rotations in the PLFMs induced either by direct current (DC) or alternating current (AC) fields. Our main results are: (i) rotation characteristics depend on the ratio $k = l_s/D$ (l_s denotes the slip length, resulting from the interface's impact on the structure of the liquid and D denotes the film's diameter). (ii) As k ($k > -1/2$) increases: (a) PLFMs subsequently exhibit rotation characteristics under "negative-", "no-", "partial-" and "perfect-" slip boundary conditions; (b) the maximum value of the linear velocity of the steady rotating liquid film increases and its location approaches the film's border; (c) the decay of the angular velocities' dependency on the distance from the center of the film slows down, resulting in a macroscopic flow near the boundary. (iii) In addition to k, the rotation characteristics of the AC PLFM depend on the magnitudes, the frequencies, and the phase difference of the AC fields. (iv) Our analytical derived rotation speed distributions are consistent with the existing experimental ones.

PACS numbers: 47.65.-d, 68.15.+e, 83.60.La, 77.22.Ej

*Corresponding author. E-mail address: phyzhqliu@163.com

I. INTRODUCTION

Exploring the physical properties, in particular hydrodynamical characteristics, of liquid films under electric, magnetic or electro-magnetic fields, is an endeavor of major theoretical and technological importance for advancements in physics, biophysics and engineering[1–4]. Currently, electro-hydro-dynamical (EHD) motions of liquid crystal films are studied intensively and their unique properties are applied widely in industry[5–8].

The recently invented suspended polar liquid film motor (PLFM) provides a good platform for studying hydrodynamics of two-dimensional fluids, as well as micro-structures of different polar liquid films, including liquid crystal films[9–12]. This motor consists of a quasi-two-dimensional electrolysis cell in an external in-plane electric field – see Fig. 1. PLFMs operating with different electric fields have important implications for micro- motors, mixers, or washers[9, 10, 13–16]; moreover, recent experiments show that a rotating suspended liquid film can be used as an electric generator[17].

In previous studies (Liu et al. Phys. Rev. E 2011, 2012), we developed models for the PLFMs which enabled quantitative and qualitative explanations for numerous experimental results, e.g., its rotation direction, threshold fields for onset of EHD and the distribution of its angular velocity[13, 14].

The impact of the PLFM's film boundaries on its EHD motions hitherto has not been addressed, i.e., all previous models assumed no-slip hydrodynamic boundary conditions at film borders[12–16, 18, 19]. However, experiments show EHD motions in PLFMs, near their films' borders, depend on polar liquid type. For example: a macroscopic observable almost static region exists near the boundary of the rotating N-(4-methoxybenzylidene)-4-butylaniline liquid crystal film[11]; for the rotating 2,5-Hexadione film, the rotation's linear velocity dependence on the distance from the center of the film decreases slowly to zero on approaching the border[10], a large linear velocity appears at the border of the rotating Benzonitrile film[10]. Moreover, recent experiments and simulations show: negative slippage exists in hydrophilic micro-channels[20] and on interfaces with a strong solid-fluid attraction[21]; numerous no-slip and partial-slip phenomena of polar liquids (e.g., water) on various solid interfaces were reported[22]; large slip effects [slip length varying from several micrometers (μm) to several hundreds μm] were observed on nanostructured superhydrophobic surfaces[23–27].

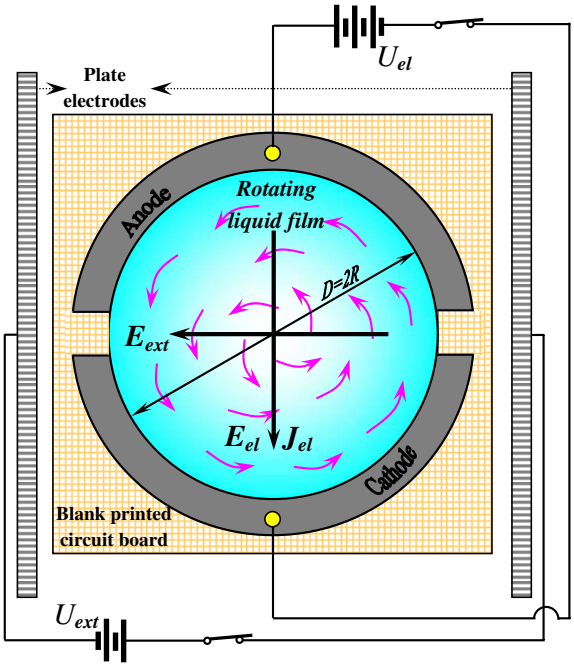

FIG. 1: (Color online) Schematic picture of the PLFM operated with DC fields. The device consists of a two dimensional frame with two graphite (or copper) electrodes (gray strips) on the sides for electrolysis of the liquid film (blue-green zone). The radius and diameter of the film are denoted, respectively, as R and D. The frame is made of an ordinary blank printed circuit board with a circular (or square) hole at the center. The diameter of the hole may vary from several centimeters to less than a millimeter. Suspended liquid films as thin as hundreds of nanometers or less may be created by brushing the liquid on the frame. The electric current $\boldsymbol{J}_{el}$ (induced by electrolysis field $\boldsymbol{E}_{el}$) and an external electric field $\boldsymbol{E}_{ext}$ are produced by two circuits with voltage U_{el} and U_{ext}, respectively. $\boldsymbol{E}_{ext}$, induced by two plates (striate strips) of a large capacitor, is perpendicular to $\boldsymbol{J}_{el}$. When the magnitudes of $\boldsymbol{E}_{el}$ and $\boldsymbol{E}_{ext}$ are above threshold values, the film rotates, i.e., constitutes a motor. The rotation direction obeys a right-hand rule, i.e., $\boldsymbol{E}_{ext} \times \boldsymbol{J}_{el}$. If the DC electric sources (bold vertical lines in circuits) are replace by AC ones, PLFM can also rotate in AC fields with the same frequencies.

The goal of our study is to investigate dynamical properties of PLFMs under slip boundary conditions. Such investigations are of theoretical, experimental and technological significance. Firstly, exploring the impact of interactions between liquids and solids on EHD motions will advance our understanding of fluid mechanics. Secondly, slippage on liquid-solid

interfaces affects fluid transportation in micro- and nano-fluidic systems:[28] large boundary slip can reduce hydrodynamic drag in micro- and nano- channels[28, 29], improving the detection efficiency of the micro-fluidic chips, i.e., the study of related mechanisms and laws is helpful to accelerate developments of lab-on-a-chip technology. Fortunately, PLFMs open new ways to explore aforementioned issues. We expect investigations on boundary slippage to elucidate several experimental boundary phenomena of various PLFMs types and to delineate optimizing methods for realizing PLFM's technological applications in the lab-on-a-chip. In this paper we focus on effects of boundary slip on rotation characteristics of PLFMs.

The outline of this paper is as follows: In Sec. II, we present a model for PLFMs with slip boundary conditions, and derive their general solutions describing their EHD motions. In Sec. III, we derive a series of specific characteristics of the DC and the AC PLFMs, and compare these with experimental ones. Our conclusions we present in Sec. IV. For convenience, the DC motor (DCM) and the AC motor (ACM) denotations are used to represent the DC and the AC PLFMs, respectively. We stress that in this paper we only theoretically derive characteristics of the DCM and the ACM under slip boundary conditions. We do not report any new experimental data. All the experimental results cited in our paper were obtained by different research groups and reported in the literature.

II. MODEL OF PLFMS WITH SLIP BOUNDARY CONDITIONS AND ITS SOLUTIONS

Our models of the DCM and the ACM, developed in previous publications[13, 14], are based on the assumption that a polar liquid film in an external electric field can be depicted as a Bingham plastic fluid with an effective electric dipole moment. Quantum field theoretical (quantum electro-dynamic) aspects of polar liquids[30–35], e.g., water, together with experimental results and their analyses, e.g., of exclusion zone (EZ) water[36, 37] and the Floating Water Bridge[38, 39], underlie this assumption – as discussed in Sec. II of reference [13] and Sec. II A of reference [14]. With our models we obtained dynamical characteristics of the DCM and the ACM with no slip boundary conditions, we successfully qualitatively and quantitatively explained many experimental phenomena and we made a series of predictions[13, 14], e.g., we predicted the EHD rotation threshold fields, the rela-

tion between the rotation speed and the phase difference of the AC fields and the vibration frequency of the ACM. Very recent experiments verified our predictions pertaining to the EHD rotations and the plastic vibrations of the ACM[12].

Encouraged by our models' previous successes, we employ these to study the slip-boundary effects on the EHD rotation properties of the DC and the AC PLFMs. In our models, inspired by the experimentally observed stable ring structure of the rotating circular (or square) liquid film, we divided the liquid film into a series of concentric cylindrical discs[13, 14], all of which obey the rotational form of Newton's second law. The dynamics equation, developed in references[13] and [14], reads

$$u_t = \frac{\mu}{\rho r^2}\left(r^2 u_{rr} + r u_r - u\right) + \frac{\Delta\left(t\right)}{\rho r}, \quad \left(0 \leq r \leq R,\, t \geq 0\right). \tag{1}$$

Here u_t denotes the first partial derivative of the linear velocity $u\left(r,t\right)$ of the disc's rotation with respect to time t; u_{rr} and u_r respectively represent the second and the first partial derivative of $u\left(r,t\right)$ with respect to the radius r, which is the average radius of a concentric cylindrical disc from r to $r+dr$; μ, ρ and $R = D/2$, respectively, are the plastic viscosity, the density and the radius of the liquid film; the driving source of the EHD rotations of the liquid film at time t is [13],

$$\Delta\left(t\right) = \varepsilon_0\left(1 - 1/\varepsilon_r\right) E_{ext}\left(t\right) E_{el}\left(t\right) \sin\theta_{EJ} - 2\tau_0, \tag{2}$$

where ε_0, ε_r and τ_0, respectively, are the dielectric constant of the vacuum, the relative dielectric constant and the yield stress of the liquid film; $E_{ext}\left(t\right)$ and $E_{el}\left(t\right)$, respectively, denote the magnitudes of the external electric field $\boldsymbol{E}_{ext}$ and of the electrolysis electric field $\boldsymbol{E}_{el}$ at time t; θ_{EJ} is the angle between $\boldsymbol{E}_{ext}$ and $\boldsymbol{E}_{el}$. Generally, $\theta_{EJ} = \pi/2$, i.e., $\boldsymbol{E}_{ext}$ is perpendicular to $\boldsymbol{E}_{el}$, as shown in Fig. 1.

In variation on our previous models, which assumed a no-slip boundary condition [i.e., $u\left(r,t\right)|_{r=R} = 0$], in the slip-boundary model of this paper, Eq. (1) should satisfy two boundary conditions and an initial condition: the disappearance of the linear velocity at $r = 0$, a nonzero slip velocity [i.e., $u_s = u\left(r,t\right)|_{r=R}$] of the linear velocity at $r = R$, and the liquid film is static at $t = 0$, i.e.,

$$u\left(r,t\right)|_{r=0} = 0, \quad u_s = -l_s u_r|_{r=R}\ , \tag{3}$$

and

$$u\left(r,t\right)|_{t=0} = 0. \tag{4}$$

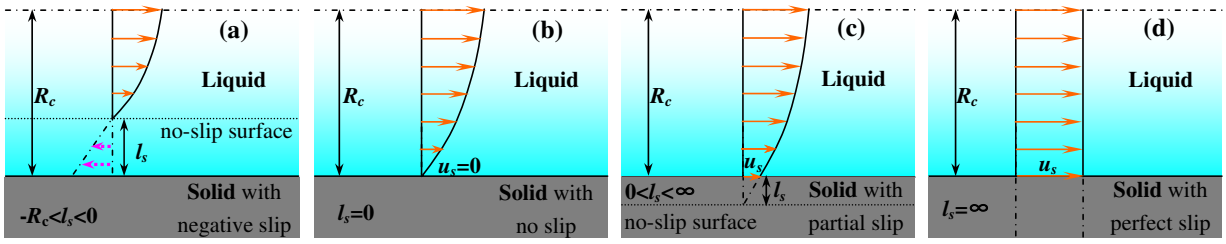

FIG. 2: (Color online) Schematic transverse cross-sections of an infinite long cylindrical channel filled with liquid, with slip boundary conditions described by different slip lengths l_s. R_c denotes the channel's radius. (a) For $-R_c < l_s < 0$, the liquid's linear velocity in the channel, i.e., $u_c(r,t)$ (represented with orange arrows) as a function of r quickly diminishes to zero in the liquid near the boundary if there is negative slip at the liquid-solid interface. Pink dotted arrows denote an imaginary reverse flow. (b) For $l_s = 0$, $u_c(r,t)$ gradually diminishes to zero near the boundary if there is no slip at the solid-liquid interface, i.e., $u_s = 0$. (c) For $0 < l_s < \infty$, when boundary slip occurs at the solid-liquid interface, there is relative velocity between fluid flow and the cylinder boundary, i.e., $u_s > 0$. (d) For $l_s = \infty$, the solid-liquid interface does not exert any resistance on the fluid, i.e., $u_c(r,t)$ is independent of r and $u_s = u_c(r,t)$. The horizontal dash-dot lines and the horizontal dotted lines represent the central line of channels and the no-slip surfaces, respectively.

Here u_s is the slip velocity of a fluid at the liquid-solid interface, u_r is the velocity gradient in a direction normal to the surface and l_s is the so-called slip length. Navier was the first to define l_s;[40] nowadays it customarily is used to characterize the type of flow in channels,[41–43] e.g., negative-slip, no-slip, partial slip and perfect-slip flows in micro- or nano- channels in lab-on-a-chip devices. For a transverse cross section of an infinite long cylindrical channel, l_s is defined as an extrapolated distance relative to its wall where the tangential velocity component vanishes (see Fig. 2c).[40, 41] Negative-slip, no-slip, partial-slip and perfect-slip conditions are described with different l_s values (see Fig. 2): if $-R_c < l_s < 0$, with R_c denoting the radius of the cylinder, the flow is negative slip flow (i.e., locking boundary)[43], see Fig. 2a; if $l_s = 0$, the flow is stick flow (i.e., no slip boundary), see Fig. 2b; if $l_s = \infty$, the flow is plug flow (i.e., perfect slip boundary), see Fig. 2d; intermediate values of l_s represent partial slip flow, see Fig. 2c. We stress that the boundary zone with the negative linear velocity in Fig. 2a does not represent the existence of a reverse flow; it may be considered as a static liquid zone;[43] its thickness in low permeability porous media is often denoted

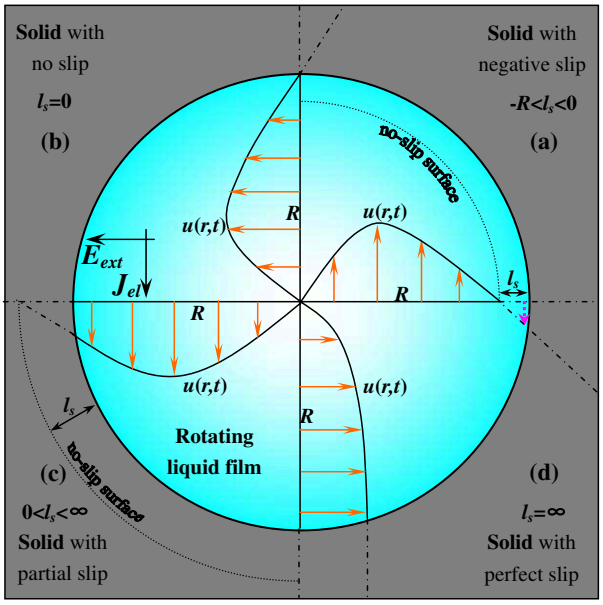

FIG. 3: (Color online) Schematic linear velocity's profiles of the slip boundary conditions, with different slip lengths l_s in a rotating liquid film. (a) $-R < l_s < 0$, negative-slip boundary; (b) $l_s = 0$, no-slip boundary; (c) $0 < l_s < \infty$, partial-slip boundary; (d) $l_s = \infty$, perfect-slip boundary.

"the boundary layer thickness".[43]

With the PLFM's suspended film corresponding to a $\sim 10^2$nm thick slice of a cylindrical channel, in our model we adopt the aforementioned definitions of l_s. The film's schematic profiles with above-defined boundary conditions are plotted in Fig. 3. Its denotations are the same as those used in Fig. 2.

Eqs. (1), (3) and (4) describe the EHD rotations of PLFMs under the above mentioned four different slip-boundary conditions described with different l_s values. The general solutions of our model's mixed problem can be obtained by the method of eigenfunctions[44]. Assuming $u(r,t) = R_f(r)\,T(t)$, inserting it into the homogeneous equation of Eq. (1) and Eq. (3), respectively, we obtain the eigenvalues problem

$$\begin{cases} R_f''(r) + R_f'(r)/r + \left(\lambda_n^2 - 1/r^2\right) R_f(r) = 0, & \text{(5a)} \\ R_f(0) = 0, \quad R_f(R) + l_s R_f'(R) = 0, & \text{(5b)} \end{cases}$$

where separation of variables method[44] was used to introduce eigenvalues λ_n . The eigenfunctions of Eq. (5), depicting the spatial modes in the general solutions of Eq. (1), are a series of the ordinary Bessel functions of order one: $J_1(\lambda_n r)$, $r \subseteq [0, R]$, $n = 1, 2, \cdots$. Obviously, $J_1(\lambda_n r)$ satisfy the first boundary condition in Eq. (5b) and the corresponding

eigenvalues $\lambda_n = \kappa_n/R$ are determined by the transcendental equation

$$J_1(\kappa_n) + \frac{l_s}{D}\kappa_n [J_0(\kappa_n) - J_2(\kappa_n)] = 0, \tag{6}$$

which is a natural result when $J_1(\lambda_n r)$ satisfy the second boundary condition in Eq. (5b). Here $J_0(\xi) - J_2(\xi) = 2J_1'(\xi)$ was used, $J_0(\xi)$ and $J_2(\xi)$, respectively, represent the Bessel functions of orders 0 and 2. For a given $k = l_s/D$, κ_n and λ_n can be obtained numerically from Eq. (6). The values of λ_n, varying with different k, determine the behaviors of $J_1(\lambda_n r)$, which reflect the spatial modes of the rotating liquid film. Therefore the rotation properties of PLFMs with the slip boundary conditions depend on k, but do not depend on the size of liquid film D and the slip length l_s.

From Eqs. (5) and (6), one may prove that the aforementioned Bessel functions $J_1(\lambda_n r)$, in variation on the functions obtained in our previous works[13, 14], should obey the following orthogonality relations (see Appendix A)

$$\int_0^R r J_1(\lambda_m r) J_1(\lambda_n r)\, dr = \frac{R^2}{2}\left[1 + \frac{1}{\lambda_n^2}\left(\frac{1}{l_s^2} - \frac{1}{R^2}\right)\right] J_1^2(\lambda_n R)\, \delta_{mn}, \tag{7}$$

where $\delta_{mn} = 1$ when $m = n$, $\delta_{mn} = 0$ when $m \neq n$. Since the above Bessel function series is a complete orthogonal system, the general solution to Eq. (1) and the last term $f(r,t) = \Delta(t)/\rho r$ in Eq. (1) may be expanded by them in generalized Fourier series, i.e.,

$$u(r,t) = \sum_{n=1}^{\infty} T_n(t) J_1(\lambda_n r), \tag{8}$$

and

$$f(r,t) = \Delta(t) \sum_{n=1}^{\infty} C_n J_1(\lambda_n r), \tag{9}$$

where

$$C_n = \frac{2\kappa_n [1 - J_0(\kappa_n)]}{R\rho [\kappa_n^2 + (R^2/l_s^2 - 1)] J_1^2(\kappa_n)}. \tag{10}$$

Inserting Eq. (8) into Eq. (3), one finds that the first boundary condition of Eq. (1) is satisfied automatically and the second one yields Eq. (6). Inserting Eqs. (8) and (9) into Eqs. (1) and (4), respectively, we have

$$T_n'(t) + a_n T_n(t) = C_n \Delta(t) \tag{11}$$

and $T_n(0) = 0$, here $a_n = \frac{\mu}{\rho}\frac{\kappa_n^2}{R^2}$. The general solution to Eq. (11) is

$$T_n(t) = e^{-a_n t}[\int C_n \Delta(t) e^{a_n t} dt + Q_n], \tag{12}$$

where the constant Q_n is determined by $T_n(0) = 0$.

Eqs. (8) and (12) present our model's general solutions for PLFMs under slip boundary conditions. The linear velocity distribution of rotating PLFMs is given by Eq. (8), in which the spatial modes and the time factors are respectively expressed by $J_1(\lambda_n r)$ satisfying Eqs. (6), (7) and by Eq. (12). The corresponding angular velocity reads

$$\omega(r,t) = u(r,t)/r. \tag{13}$$

III. RESULTS AND DISCUSSION

PLFMs can work perfectly with many different crossing electric fields, e.g., DC[9, 10, 13], AC[9, 14], square-wave[15] and other type[16]. In this study, we present the boundary slip effects on the rotation properties of PLFMs operated with DC and AC fields, and compare these with experimentally observed results.

A. DCM with slip boundary conditions

According to Eq. (2), for DCM $\Delta(t)$ is a constant, i.e., independent of time t:

$$\Delta^{dc} = \Delta(t) = \varepsilon_0 (1 - 1/\varepsilon_r) E_{ext} E_{el} \sin\theta_{EJ} - 2\tau_0. \tag{14}$$

On inserting Eq. (14) into Eq. (12), we obtain the time factors describing the rotation evolution of the DCM:

$$T_n^{dc}(t) = \frac{C_n \Delta^{dc}}{a_n}\left(1 - e^{-a_n t}\right). \tag{15}$$

From Eqs. (8), (10) and (15), we obtain the linear velocity of the DCM

$$u^{dc}(r,t) = \sum_{n=1}^{\infty} C_n^{dc} J_1\left(\frac{\kappa_n r}{R}\right)\left(1 - e^{-a_n t}\right), \tag{16}$$

where

$$C_n^{dc} = \frac{2R\Delta^{dc}}{\mu} \frac{1 - J_0(\kappa_n)}{\kappa_n \left[\kappa_n^2 + (R^2/l_s^2 - 1)\right] J_1^2(\kappa_n)} \tag{17}$$

The corresponding angular velocity is given by Eqs. (13) and (16).

To illuminate the dynamical characteristics of the DCM for different k values, we adopt the experimental parameters of the exemplary extensively measured and theoretically investigated DCM[9, 10, 13, 14], i.e.: $\varepsilon_0 = 8.85 \times 10^{-12}$ F·m^{-1}, $\varepsilon_r = 80$, $E_{ext} U_{el} \sin\theta_{EJ} = 7.2 \times 10^6$

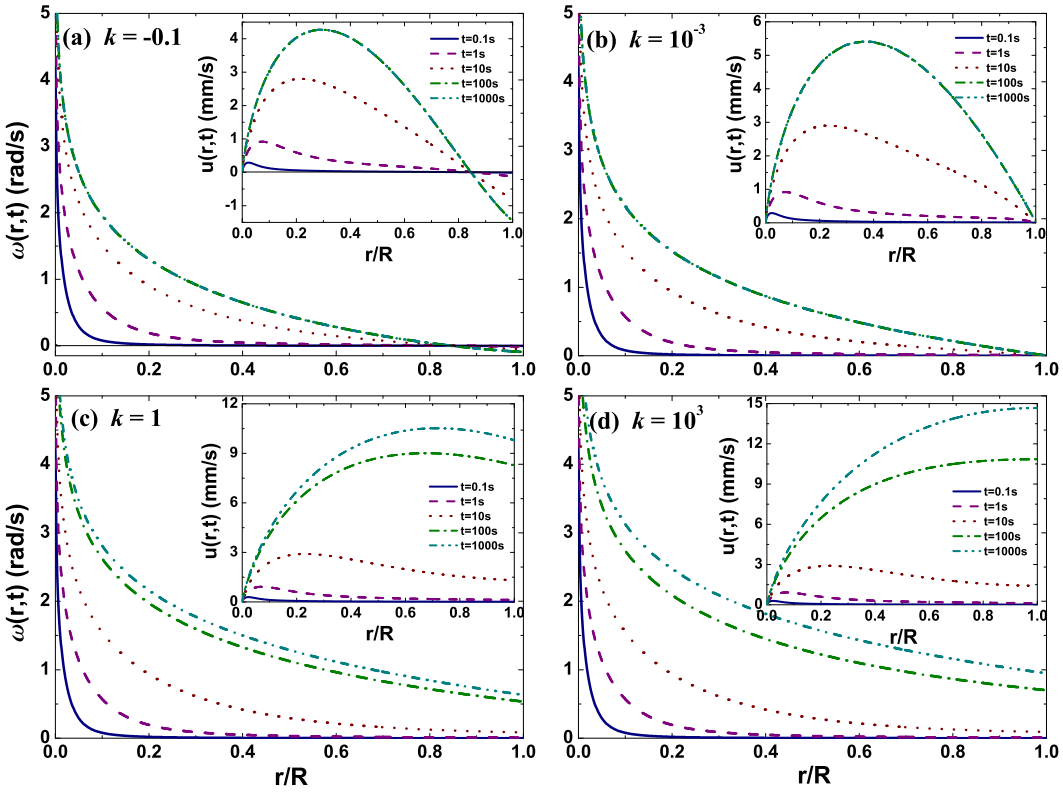

FIG. 4: (Color online) The profiles of the angular velocity of the DCM with four different boundary conditions represented by different values of k at different times: (a) $k = -0.1$; (b) $k = 10^{-3}$; (c) $k = 1$; (d) $k = 10^3$. The insets show the profiles of the corresponding linear velocity of each figure.

$\mathrm{V}^2{\cdot}\mathrm{m}^{-1}$, $D = 2R = 3.1 \times 10^{-2}$ m, $\rho = 10^3$ kg·m^{-3}, $\mu = 10^{-3}$ Pa·s and its derived $\tau_0 = 6.77 \times 10^{-5}$ Pa. With these parameters, we investigated characteristics of the angular and linear velocities dependencies on k. We found that by setting $k = -0.1$, 10^{-3}, 1 or 10^3, the DCM rotates under, respectively, negative-slip, approximately-no-slip, partial-slip and approximately-perfect-slip boundary conditions, as discernible from Fig. 4: This figure depicts the profiles of our computed angular and linear velocities at different times – by drawing the intersection points of the tangent lines to the curves with $t = 1000$s at the point R and the horizontal axis in the insets of Fig. 4, it is noticeable that Figs. 4a-d are consistent with the four slip boundary cases presented by Figs. 3a-d, respectively. To illustrate this more clearly, we plot the profiles of the steady rotation angular velocities of the DCM in Fig. 5a. The main rotation characteristics of the DCM, observable from Figs. 4 and 5a, are:

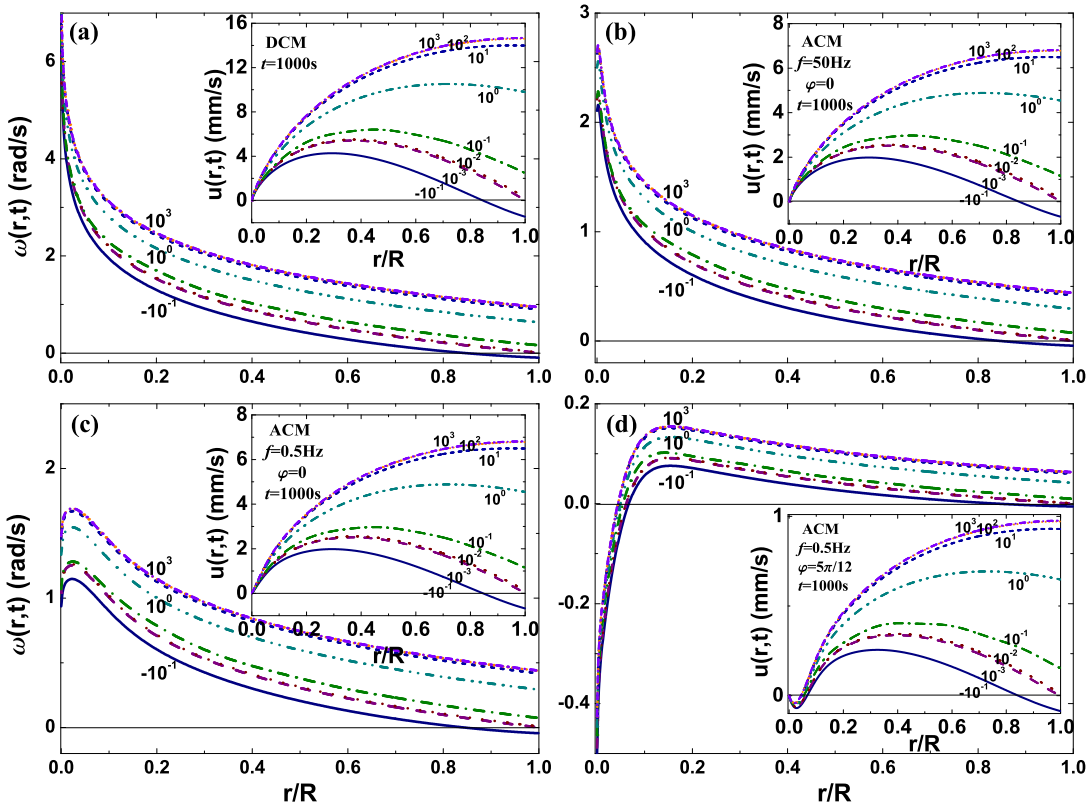

FIG. 5: (Color online) The profiles of the angular velocity of the steady rotating DCM and ACM with different k values. k varies from -0.1 to 10^3. (a) DCM; (b) ACM with $f = 50$Hz and $\varphi = 0$; (c) ACM with $f = 0.5$Hz and $\varphi = 0$; (d) ACM with $f = 0.5$Hz and $\varphi = 5\pi/12$. The insets show the profiles of the corresponding linear velocity of each figure. Obviously, the rotation properties of the DCM depend on k, while those of the ACM are associated with k as well as these depend on the frequencies and on the phase difference of the AC fields.

(i) The points near the center of the film, independent of the boundary conditions, start to rotate earlier than those farther away from it. This derived result is in full agreement with the experimental one.[9, 10]

(ii) For any k, the angular velocities decrease with increasing r, i.e., these are smaller at points further away from the film's center – see Fig. 4. This prediction too fully agrees with the experimental ones.[9, 10]

(iii) As k increases, the angular velocity of the steady rotation grows gradually and its decay rate with r deceases slowly. Experiments capable of verifying this prediction have not yet been reported and are called for.

(iv) The linear velocity's distribution mainly depends on the ratio k, but not on the particular values of R and l_s, i.e., it exhibits significant different characteristics as k increases. For some k values, the linear velocity distributions are qualitatively consistent with experimental ones, as we discuss in the next paragraphs a-d.

a. For $-1/2 < k < 0$, the DCM rotates under a negative slip boundary condition, i.e., locking boundary – see Fig. 4a which shows that as r increases from zero (i.e., from the center of the film), the rotation's linear velocity increases quickly from zero to a maximum and then decreases slowly to zero, even to a negative value as r increases further.

As mentioned in Sec. II, the zone around a border with negative linear velocity (see pink dashed arrows in Figs. 2a and 3a) may be considered as a zone with static liquid. Simulation with the lattice Boltzmann method show that a strong solid-fluid attraction may result in a small negative slip length[21]. Molecular dynamics simulations show that the no-slip or locking boundary conditions correspond to ordered liquid structures close to the solid walls leading to zero and negative slip lengths, respectively[45]. Strong solid-fluid attractions and ordered liquid structures close to the solid walls have been observed in numerous recent experiments: A wide zone of long-ordered, high-viscosity and liquid-crystal-phase water adjacent to objects like hydrophilic membranes, reactive metal sheets, biological tissues, optical fibers, gels with charged or uncharged surfaces has been observed[36].

Combining the experimental and simulations' results cited in the last paragraph with our theoretical ones, we predict that the DCM may exhibit a physics picture given by Fig. 4a when motor's frames are made of hydrophilic materials. This conjecture is partly supported by the experimental results of rotating liquid crystal films driven by crossing DC electric fields:[11] Figure 4a in this paper is qualitatively consistent with Figs. 2d and 5 in reference [11]. Since water and liquid crystals have different micro-structures and properties, further experiments are called for to verify the above prediction and more detailed theoretical investigations are needed.

b. For k a small positive number, e.g. $0 < k \leq 10^{-2}$, the DCM rotates under an approximately-no-slip condition – Figs. 4b and 5a show that the rotation properties of the DCM are almost the same as those obtained on assuming no slip boundary condition, see Figs. 7 and 8 of Ref. [13]. The linear velocity has its maximum at R/e, with e representing the irrational and transcendental constant approximately equal to 2.71828, and the angular velocity is a decreasing function of the radius r. This result shows that the slip boundary

effect may be ignored when the slip length l_s is much less than the size of the liquid film. It also indirectly proves that our model is reasonable.

c. For $10^{-2} < k <\sim 10$, the DCM rotates under partial slip condition – we can discern this result by drawing the intersection points of the tangent lines to the curves at the point $r/R = 1$ and the horizontal axis in the insets of Figs. 4 and 5a, and subsequently compare with Fig. 3c. As k increases above 10^{-2}, the maximum value of the linear velocity of the steady rotating liquid film increases and its location moves from R/e to R, as shown in Fig. 5a.

For the magnitudes of the external electric fields and solid-liquid border parameters, adopted above for our exemplary DCM, it is reasonable to assume l_s is constant. Thus, Fig. 5a indicates that the linear and angular velocities will increase as the size of the liquid film decreases. It is also noteworthy that for $k = 1$ and $t = 1000$s, the maximum value of the linear velocity locates around $2R/e$, the angular velocity decays slowly with increasing r and it has a large value at the boundary (see Fig. 4c). These properties are qualitatively consistent with the experimental ones exhibited by the rotating Benzonitrile film (see Fig. 3c in reference [10]). Hence investigating the slip boundary effects facilitates understanding some experimental results unexplainable with our previous model[13], which did not treat slip boundaries.

d. For sufficient large k, e.g., $k \geq 10$ (see Fig. 5a), the DCM rotates under approximately-perfect-slip boundary condition – we can obtain this result by the same method mentioned in case c. The angular velocity is a decreasing function of the radius r (see Fig. 4d) and the linear velocity of steady rotation is an increasing function of the radius r (see the inset in Fig. 4d). To the best of our knowledge, hitherto, there are no corresponding experimental results for verifying these theoretical ones.

B. ACM with slip boundary conditions

Experimental[9, 12] and our previously published theoretical results[14] show: when the crossing AC fields have the same frequencies, the ACM exhibits rotation characteristics similar to those of the DCM; AC fields with different frequencies can merely induce vibrations not rotation. Our detailed previously published predictions on ACM's rotation and vibration characteristics[14] are now fully confirmed by experiments[12], with the exception of some

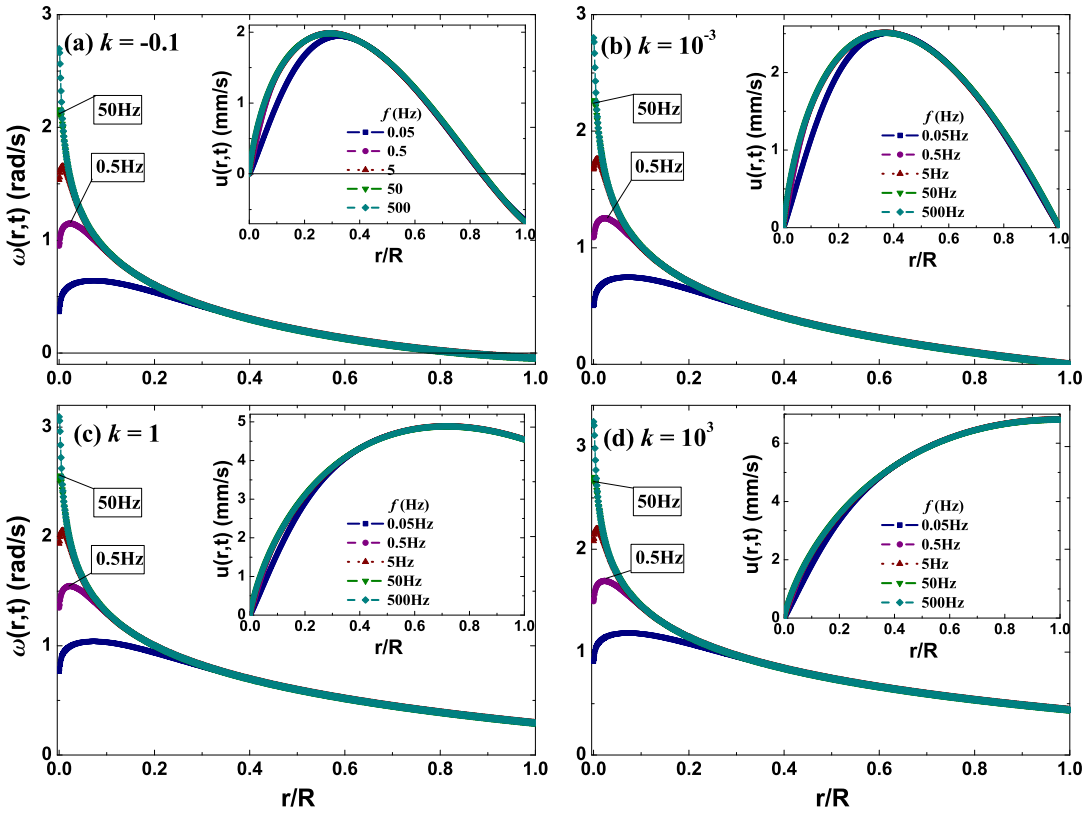

FIG. 6: (Color online) The profiles of the angular velocity of the steady rotating ACM with different values of f for $\varphi = 0$ at time $t = 1000$s. f varies from 0.05 Hz to 500Hz. (a) $k = -0.1$; (b) $k = 10^{-3}$; (c) $k = 1$; (d) $k = 10^{3}$. The insets show the profiles of the corresponding linear velocity of each figure. Obviously, the rotation properties around the film's center depend on f, while those near the film's boundary are associated with k. As f decreases, the angular velocities vary from a monotonically decreasing function to a first increasing then decreasing function. As k increases, the ACM subsequently exhibits negative-slip, no-slip, partial-slip, perfect-slip behaviors.

details of the elastic vibration – a model based on our previous published one, with the improvement of assuming the film to be an elastic Bingham fluid, explains these details[12]. In the model presented in this paper, we did not include the aforementioned improvement, i.e., we do not expect it to describe all vibration properties of ACMs. Still, based on its previous success in correctly describing ACMs' rotation properties, we conjecture our model can elucidate the effect of slip boundaries on the ACM rotations.

For the analysis we define the alternating external electric field and electrolysis voltage, respectively, as $E_{ext}(t) = E_0 \sin \omega^{ac} t$ and $U_{el}(t) = E_{el}(t) D = U_0 \sin(\omega^{ac} t + \varphi)$. Here E_0

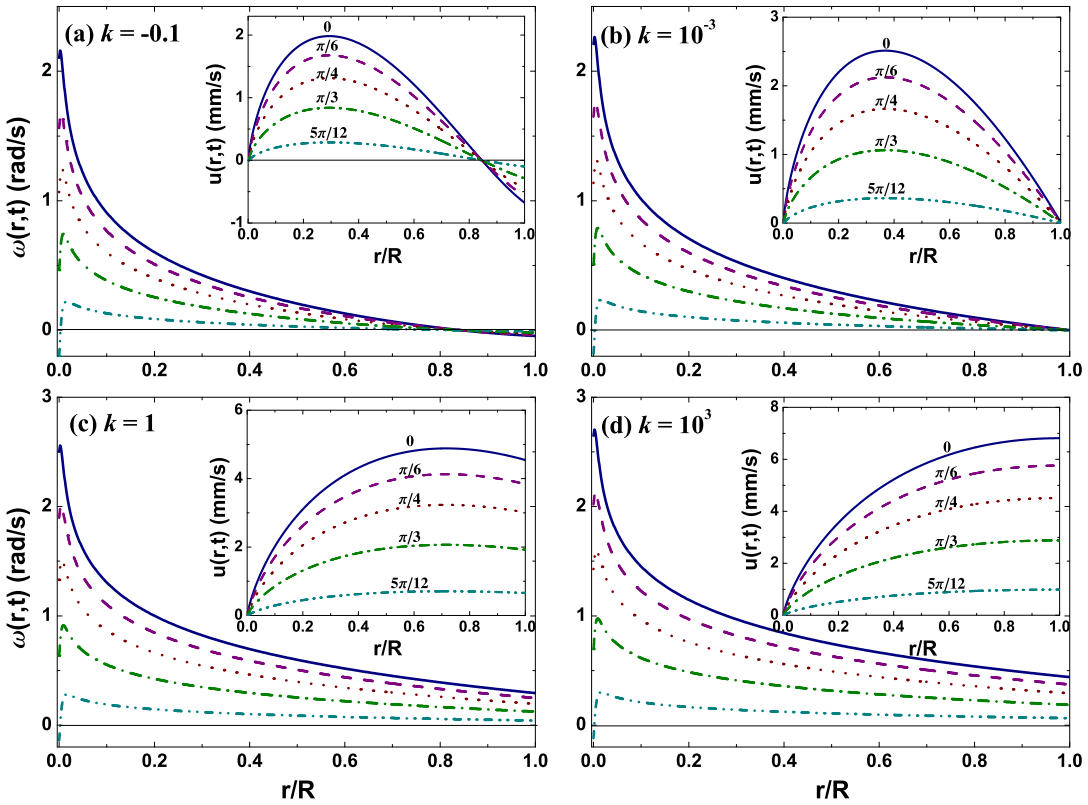

FIG. 7: (Color online) The profiles of the angular velocity of the rotating ACM with different k values for various values of φ ($\varphi = 0$, $\pi/6$, $\pi/4$, $\pi/3$, $5\pi/12$) at time $t = 1000$s: (a) $k = -0.1$; (b) $k = 10^{-3}$; (c) $k = 1$; (d) $k = 10^{3}$. The frequencies of the AC fields are 50Hz. The insets show the profiles of the corresponding linear velocity of each figure. Obviously, the angular velocities are decreasing functions of the radius. On comparing curves in this figure with those with $t = 1000$s in Fig. 4, for the corresponding k values, one finds that the ACM and the DCM exhibit similar characteristics when AC fields' frequencies are large (e.g., $f = 50$Hz). As φ increases, the rotation speed decreases gradually.

and U_0, respectively, denote the amplitudes of the electric field and the voltage, $\omega^{ac} = 2\pi f$ represents their angular frequencies, φ is the initial phase of the electrolysis voltage and it also represents the phase difference between the AC fields. From Eq. (2), we obtain the source driving the rotation of the ACM (as explicitly shown in Ref. [14] – Sec. III B)

$$\Delta^{ac}(t) = B_c + B_t = (b^{ac}\cos\varphi - 2\tau_0) - b^{ac}\cos(2\omega^{ac}t + \varphi), \tag{18}$$

where $b^{ac} = \frac{\varepsilon_0(1-1/\varepsilon_r)E_0U_0\sin\theta_{EJ}}{4R}$. Eq. (18) is suitable for studying the rotation of the ACM

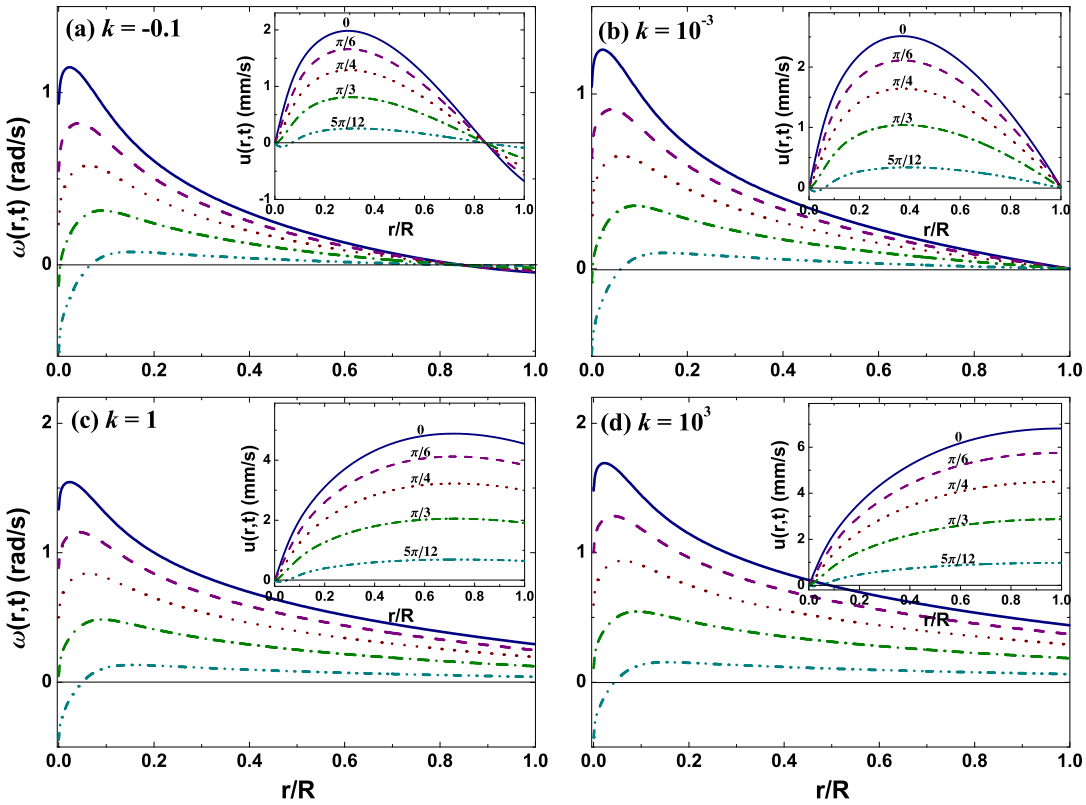

FIG. 8: (Color online) The profiles of the angular velocity of the rotating ACM with different k values for various values of φ ($\varphi = 0$, $\pi/6$, $\pi/4$, $\pi/3$, $5\pi/12$) at time $t = 1000$s: (a) $k = -0.1$; (b) $k = 10^{-3}$; (c) $k = 1$; (d) $k = 10^{3}$. The insets show the profiles of the corresponding linear velocity of each figure. The frequencies of the AC fields are 0.5Hz. As φ increases, the rotation speed not only decreases gradually, but also its maximum moves away from the center of the film.

only if $B_c > 0$, which means the active torque should first destroy the plastic structure of the liquid film before it can induce the film to rotate. Inserting Eq. (18) into Eq. (12), we obtain the time factors describing the evolution of the ACM, i.e.,

$$T_n^{ac}(t) = C_n^{acBc}\left(1 - e^{-a_n t}\right) + C_n^{acBt}\cos\gamma_n\left[\cos\left(\varphi - \gamma_n\right)e^{-a_n t} - \cos\left(2\omega^{ac}t + \varphi - \gamma_n\right)\right], \quad (19)$$

where $C_n^{acBc} = C_n B_c/a_n$, $C_n^{acBt} = C_n b^{ac}/a_n$, $\gamma_n = \arctan\left(2\omega^{ac}/a_n\right)$. By employing Eqs. (8)

and (19), we have

$$u^{ac}(r,t) = \sum_{n=1}^{\infty} C_n^{acBc} J_1\left(\frac{\kappa_n r}{R}\right)\left(1-e^{-a_n t}\right) + \sum_{n=1}^{\infty} C_n^{acBt} J_1\left(\frac{\kappa_n r}{R}\right)\cos\gamma_n\left[\cos\left(\varphi-\gamma_n\right)e^{-a_n t} - \cos\left(2\omega^{ac}t+\varphi-\gamma_n\right)\right]. \quad (20)$$

The corresponding angular velocity is given by Eqs. (13) and (20). Eq. (20) indicates that for the ACM, rotation of the film comprises not only rotation modes but also plastic vibration modes. Our calculations, reported in the following paragraphs, show the contributions of these two different types of modes vary with the magnitudes, the frequencies and the phase difference of the AC fields. Thus, the dynamical characteristics of the ACM with slip boundary conditions depend on k as well as on the aforementioned variables. Obviously, Eqs. (18) and (20) show that the rotation speed increases as the AC fields' magnitudes increase, because higher fields induce larger average active torque in the film. The aforementioned results agree well with the experimental ones: measurements show that in the case of phase differences, vibration and rotation exist simultaneously and by increasing the magnitude of the electric fields, the ratio between vibration and rotation velocities changes. In high electric fields the rotation dominates, while in lower fields the vibration dominates[12].

To illuminate in detail the dynamical characteristics of the ACM for different k, f and φ values, we adopt in the expression for b^{ac} [employed in Eq.(18)] $E_0 U_0 \sin\theta_{EJ} = 7.2 \times 10^6$ $\mathrm{V^2 \cdot m^{-1}}$, i.e., the same value as that used in our previous analyses [14]; for the other parameters we adopt the values of the DCM of Section III A. With Eqs. (13) and (20), we computed numerous profiles of the angular velocity of the steady rotating ACM for different k, f and φ values and in depth analyzed these. Exemplary cases, which depict the main trends, we plot in Figs. 5b-d, 6-8.

From Figs. 5b-d – which exhibit the profiles of the angular and linear velocity of the steady rotating ACM with different k values (k varies from -0.1 to 10^3) for the three cases of $f = 50$Hz and $\varphi = 0$, of $f = 0.5$Hz and $\varphi = 0$ and of $f = 0.5$Hz and $\varphi = 5\pi/12$ – we learn:

(i) The boundary dynamical behaviors of the ACM, just as those of the DCM studied earlier in Sec. III A, are determined by k: On comparing Figs. 5b-d with Fig. 3, it is discernible that as k increases ACM subsequently exhibits "negative-", "no-", "partial-" and "perfect-" slip behaviors. To the best of our knowledge, neither experimental nor

computational data have been reported that can verify Fig.5's predictions, i.e., creation of such data is called for.

(ii) For given AC fields' magnitudes, the contributions of rotation modes and plastic vibration modes depends on f and φ:

a. For high f and small φ, e.g., $f \geq 50$Hz and $\varphi = 0$, the ACM exhibits characteristics similar to those of the DCM: All the angular velocities are almost monotonically decreasing functions of r and all the linear velocities increase with increasing k – as can be seen by comparing Fig. 5a with 5b. These theoretical results agree well with the experimental ones: the measured dynamical characteristics of the rotation of the ACM, for frequencies in the range of 50Hz up to 40kHz, are the same as those of the DCM[9].

b. For low f and small φ, e.g., $f \leq 0.5$Hz and $\varphi = 0$, the ACM and the DCM exhibit different properties. The angular velocities of the ACM do not monotonically decrease with r, as do those of the DCM – as can be seen by comparing Fig. 5a with 5c. The ACM's angular velocities increase first and then decrease as r enhances. Moreover, our computations show that the location of the maximum of the angular velocity moves away from the center of the liquid film as the AC fields' frequencies decrease, see Fig. 6. The underlying physical reason for this dependency of the ACM's angular velocities on r is that the contributions of the plastic vibration modes to the linear velocity increase as AC fields' frequencies decrease. When the frequencies are higher, the minor and faster plastic vibrations, arising from the second term of Eq. (18), can not induce a macroscopic flow in the liquid film in each half period of $T_1 = 1/(2f)$. As f decreases, the plastic vibration modes' ability to produce a macroscopic reverse flow in the liquid film strengthens and leads to the velocities presented in Figs. 5c, 6 and 8. These theoretical results agree well with the numerical ones given in Fig. 6 of reference [12], which show that as frequencies increase, the plastic vibration gets weaker.

c. For large φ and low f values, e.g., $\varphi = 5\pi/12$ and $f = 0.5$Hz (see Fig. 5d), the ACM exhibit an interesting phenomenon: the region near the center of the film and that near the border may rotate in opposite directions. The underlying reason is that as φ increases, $B_c = (b^{ac}\cos\varphi - 2\tau_0)$ in Eq. (18) decreases. This leads to a diminishment of the rotation modes' contributions to the EHD motions in the ACM, while those of vibration modes become more distinct. To the best of our knowledge, hitherto, there are no corresponding experimental results for verifying these theoretical ones.

Detailed effects of φ on the rotation characteristics of the ACM we present in Figs. 7 and 8. These figures show that the rotation speed of the ACM decreases as φ increases. Moreover, these show when f is high enough, the positional deviation of the maximum of the angular velocity from the center of the film is negligible with increasing φ, see Fig. 7. However, when f is small, this deviation becomes significant as φ increases: When φ is large enough, the region near the center of the film and that near the border may rotate in opposite directions (see curves with $\varphi = 5\pi/12$ in Fig. 8). The aforementioned theoretical results agree with the experimental and calculated ones[12]: Experimental results show that average tangential velocities of an ACM, with a phase difference of $\varphi = 5\pi/12 = 75^0$, frequency of 41Hz and $E_{ext0}E_{el0} = 2.2 \times 10^8$ V^2·m^{-2}, may be positive or negative – see Fig. 3 in reference [12]; Calculated results of shear rates show that the average values of the plastic shear rate and the rotatory shear rate are opposite in sign – see the bottom picture of Fig. 5 in reference [12].

IV. SUMMARY AND CONCLUSIONS

By introducing slip boundary conditions in the DCM and ACM models (developed by us in our previous publications),[13, 14] we investigated their rotation characteristics for different slip boundary types. To the best of our knowledge, our study is the first to theoretically derive slip boundary effects on these PLFM's EHD.

Our computations with our slip boundary DCM and ACM models, for small boundary slip length l_s, i.e., approximately-no-slip condition, respectively, recover the dynamical characteristics of the DCM and the ACM with no-slip boundary condition. Our computations also present the rotation properties of these motors with negative-slip, partial-slip and perfect-slip conditions. These properties shed light on several experimentally observed rotation characteristics of the DCM and ACM at their borders. Our theoretically derived properties agree with the existing experimental ones and those obtained with numerical techniques. Additional experiments, required for verifying our remaining derived properties which are specified in Sec. III A and B, are called for.

One of our central theoretical results is that the rotation speed distributions are independent of the absolute values of the l_s and the liquid film's diameter D, but are associated with their ratio $k = l_s/D$:

(i) As k ($k > -1/2$) increases, DCM and ACM subsequently exhibit rotation characteristics under "negative-", "no-", "partial-" and "perfect-" slip boundary conditions;

(ii) For the DCM, k affects the magnitude of its linear velocity: for small k values, this magnitude first increases and then decreases with the radius r of the liquid film at its steady rotation; as k increases, this magnitude increases and the location of its maximum approaches the film's boundary. As to the effects of k on the DCM's angular velocity: for any k, it always decays with r; as k increases, its decay rate slows down, and this results in a nonzero angular velocity at the border of the liquid film.

(iii) For the ACM, its EHD motions depends on k, as well as on the magnitude, frequencies and phase difference of the AC fields; moreover these motions comprise rotation modes and plastic vibration modes. At high frequencies, the ACM exhibits similar rotation characteristics to the DCM with the same k. At low-frequency, its rotation properties distinctly differ from those of the DCM, because the plastic vibration may weaken the rotation around the film's center – as a result the region near the center of the film and that near the border even may rotate in opposite directions when the phase difference is large enough.

As to desirable future research, we note that the slip length l_s was introduced into our model to study the effects of slip boundary on the dynamical properties of the DCM and the ACM. However, we did not study any factors affecting the values of l_s, such as the solid-fluid potential interactions, surface roughness, wettability[41], the presence of gaseous layers[26, 46] and dipole moment of polar liquids[47]. As such, future research on factors affecting l_s is called for. In particular, because as mentioned in Sec. I, for example, the nano-structured super-hydrophobic surface can produce large slip length in the solid-liquid interface[23–27]. We expect large l_s to accelerate mixing effects of PLFMs – for PLFMs operating at high rotational speeds induced by identical external electric fields, large l_s seems to be of special importance for optimizing the micro-mixer investigated in one of our previous studies[15].

We conclude with mentioning: the study of water slippage on different interfaces has always been an important and even a hot issue[22, 41]; our study indicates that fabricating PLFMs with different hydrophilic or hydrophobic frames offers opportunities for studying the solid-liquid interfacial slippage; we expect such a study to deepen our understanding of the dynamical properties of the PLFMs; we anticipate that such investigation ultimately will lead to delineation of those film characteristics required for optimizing the PLFMs.

Appendix A: Orthogonality relations among $J_1(\lambda_n r)$

The first differential equation in Eq. (5) may be simplified as

$$\frac{d}{dr}\left(r\frac{dR_f}{dr}\right)+\left(\lambda^2 r-\frac{1}{r}\right)R_f=0. \tag{A1}$$

If $m\neq n$, $\lambda_m\neq\lambda_n$, inserting $J_1(\lambda_n r)$ and $J_1(\lambda_m r)$ into Eq. (A1), respectively, we obtain

$$\frac{d}{dr}\left(r\frac{dJ_1(\lambda_n r)}{dr}\right)+\left(\lambda_n^2 r-\frac{1}{r}\right)J_1(\lambda_n r)=0, \tag{A2}$$

$$\frac{d}{dr}\left(r\frac{dJ_1(\lambda_m r)}{dr}\right)+\left(\lambda_m^2 r-\frac{1}{r}\right)J_1(\lambda_m r)=0. \tag{A3}$$

Let $J_1(\lambda_m r)$ multiply Eq. (A2), $J_1(\lambda_n r)$ multiply Eq. (A3), and the former minus the latter, then calculate the integral of them from 0 to R, we obtain

$$\left(\lambda_n^2-\lambda_m^2\right)\int_0^R rJ_1(\lambda_m r)J_1(\lambda_n r)\,dr=J_1(\lambda_n R)\lambda_m RJ_1^{'}(\lambda_m R)-J_1(\lambda_m R)\lambda_n RJ_1^{'}(\lambda_n R). \tag{A4}$$

Since λ_n and λ_m should satisfy Eq. (6), we obtain

$$\lambda_n RJ_1^{'}(\lambda_n R)=-\frac{R}{l_s}J_1(\lambda_n R),\ \lambda_m RJ_1^{'}(\lambda_m R)=-\frac{R}{l_s}J_1(\lambda_m R). \tag{A5}$$

On inserting Eq. (A5) into Eq. (A4), one finds for $m\neq n$,

$$\int_0^R rJ_1(\lambda_m r)J_1(\lambda_n r)\,dr=0. \tag{A6}$$

Next, let us discuss the case $m=n$. When $m\to n$, i.e., when $\lambda_m\to\lambda_n$, if λ_n satisfies the first equation in Eq. (A5), λ_m does not satisfy the second equation in Eq. (A5), i.e., $\lambda_m RJ_1^{'}(\lambda_m R)\neq-\frac{R}{l_s}J_1(\lambda_m R)$. As $m\to n$, from Eq. (A4) we have

$$\int_0^R rJ_1(\lambda_m r)J_1(\lambda_n r)\,dr=\lim_{\lambda_m\to\lambda_n}\frac{J_1(\lambda_n R)\lambda_m RJ_1^{'}(\lambda_m R)+\frac{R}{l_s}J_1(\lambda_m R)J_1(\lambda_n R)}{\lambda_n^2-\lambda_m^2}. \tag{A7}$$

Applying L Hospital rule to the right hand of Eq. (A7), i.e., deducing the derivative of the numerator and denominator with respect to λ_m, respectively, we obtain

$$\int_0^R rJ_1^2(\lambda_n r)\,dr=-\frac{R^2J_1(\lambda_n R)}{2\lambda_n^2}\left[\lambda_n J_1^{'}(\lambda_n R)/R+\lambda_n^2 J_1^{''}(\lambda_n R)+\lambda_n J_1^{'}(\lambda_n R)/l_s\right]. \tag{A8}$$

From Eq. (A2) and the first equation of (A5), we obtain $\lambda_n^2 J_1^{''}(\lambda_n R)=-\lambda_n J_1^{'}(\lambda_n R)/R-(\lambda_n^2-1/R^2)J_1(\lambda_n R)$, and $\lambda_n J_1^{'}(\lambda_n R)=-J_1(\lambda_n R)/l_s$. Inserting them into Eq. (A8), we obtain

$$\int_0^R rJ_1^2(\lambda_n r)\,dr=\frac{R^2}{2}\left[1+\frac{1}{\lambda_n^2}\left(\frac{1}{l_s^2}-\frac{1}{R^2}\right)\right]J_1^2(\lambda_n R). \tag{A9}$$

Combining Eq. (A6) with Eq. (A9), we obtain the orthogonality relations given by Eq. (7).

Acknowledgments

Our work has been supported by National Natural Science Foundation of China (No. 11302118), Natural Science foundation of Shandong Province (No. ZR2013AQ015) and the Science Foundation of Qufu Normal University (No. BSQD2012053). Tamar Yinnon expresses her appreciation for Prof. A. M. Yinnon's continuous support and encouragement.

---

[1] R. A. L. Jones, Soft condensed matter (Oxford University Press, New York 2002).

[2] P. Nelson, Biological physics: energy, information, life (W. H. Freeman, New York 2003).

[3] T. M. Squires and S. R. Quake, Rev. Mod. Phys. **77**, 977 (2005).

[4] H.-C. Chang and L. Y. Yeo, Electrokinetically-driven microfluidics and nanofluidics (Cambridge University Press, New York 2010).

[5] A. A. Sonin, Freely Suspended Liquid Crystalline Films (John Wiley and Sons, New York 1998).

[6] S. Faetti, L. Fronzoni, and P. A. Rolla, J. Chem. Phys. **79**, 5054 (1983).

[7] S. W. Morris, J. R. de Bruyn, and A. D. May, Phys. Rev. Lett. **65**, 2378 (1990).

[8] Z. A. Daya, S. W. Morris, and J. R. de Bruyn, Phys. Rev. E **55**, 2682 (1997).

[9] A. Amjadi, R. Shirsavar, N. H. Radja, and M. R. Ejtehadi, Microfluid Nanofluid **6**, 711 (2009).

[10] R. Shirsavar, A. Amjadi, A. Tonddast-Navaei, and M. R. Ejtehadi, Exp. Fluids **50**, 419 (2011).

[11] R. Shirsavar, A. Amjadi, M. R. Ejtehadi, M. R. Mozaffari, and M. S. Feiz, Microfluid Nanofluid **13**, 83 (2012).

[12] A. Amjadi, R. Nazifi, R. M. Namin, and M. Mokhtarzadeh, arXiv:1305.1779v1 (2013).

[13] Z.-Q. Liu, Y.-J. Li, G.-C. Zhang, and S.-R. Jiang, Phys. Rev. E **83**, 026303 (2011).

[14] Z.-Q. Liu, G.-C. Zhang, Y.-J. Li, and S.-R. Jiang, Phys. Rev. E **85**, 036314 (2012).

[15] Z.-Q. Liu, Y.-J. Li, K.-Y. Gan, S.-R. Jiang, and G.-C. Zhang, Microfluid Nanofluid **14**, 319 (2013).

[16] Z.-Q. Liu, K.-Y. Gan, Y.-J. Li, G.-C. Zhang, and S.-R. Jiang, Acta Phys. Sin. **61**, 134703 (2012).

[17] A. Amjadi, S. Feiz, and R. M. Namin, arXiv:1305.7165v1 (2013).

[18] E. V. Shiryaeva, V. A. Vladimirov, and M. Y. Zhukov, Phys. Rev. E **80**, 041603 (2009).

[19] F. P. Grosu and M. K. Bologa, Surface Engineering and Applied Electrochemistry **46**, 43 (2010).

[20] F.-Q. Song and L. Yu, Advanced Materials Research **594-597**, 2684 (2012).

[21] J.-F. Zhang and D. Y. Kwok, Phys. Rev. E **70**, 056701 (2004).

[22] E. Lauga, M. P. Brenner, and H. A. Stone, in Handbook of Experimental Fluid Dynamics, Chapter 19. C. Tropea, A. Yarin, J. F. Foss (Eds.) Springer, (2007).

[23] P. Joseph, C. Cottin-Bizonne, J.-M. Benoît, C. Ybert, C. Journet, P. Tabeling, and L. Bocquet, Phys. Rev. Lett. **97**, 156104 (2006).

[24] C.-H. Choi and C.-J. Kim, Phys. Rev. Lett. **96**, 066001 (2006).

[25] C. Lee, C.-H. Choi, and C.-J. Kim, Phys. Rev. Lett. **101**, 064501 (2008).

[26] E. Karatay, A. S. Haase, C. W. Visser, C. Sun, D. Lohse, P. A. Tsai, and R. G. Lammertink, Proc. Natl. Acad. Sci. U.S.A. **110**, 8422 (2013).

[27] Y. Wu, M.-R. Cai, Z.-Q. Li, X.-W. Song, H.-Y. Wang, X.-W. Pei, and F. Zhou, Journal of Colloid and Interface Science **414**, 9 (2014).

[28] L. Bocquet and E. Charlaix, Chem. Soc. Rev. **39**, 1073 (2010).

[29] J.-L. Barrat and L. Bocquet, Phys. Rev. Lett. **82** 4671 (1999); J. Baudry, E. Charlaix, A. Tonck, and D. Mazuyer, Langmuir **17** 5232 (2001); D. C. Tretheway and C. D. Meinhart, Phys. Fluids **14** L9 (2002); E. Lauga and M. P. Brenner, Phys. Rev. E **70** 26311 (2004); C. H. Choi and C. J. Kim, Phys. Rev. Lett. **96**, 066001 (2006); Y. Wu, M.-R. Cai, Z.-Q Li, X.-W. Song, H.-Y. Wang, X.-W Pei, and F. Zhou, Journal of Colloid and Interface Science **414**, 9 (2014).

[30] E. Del Giudice, G. Preparata, and G. Vitiello, Phys. Rev. Lett. **61**, 1085 (1988).

[31] S. Sivasubramanian, A. Widom, and Y. N. Srivastava, Physica A **345**, 356 (2005); E. Del Giudice and G. Vitiello, Phys. Rev. A **74**, 022105 (2006).

[32] G. Preparata, QED Coherence in Matter (World Scientific, Singapore, New Jersey, London, Hong Kong 1995); G. Preparata, Phys. Rev. A **38**, 233 (1988); R. Arani, I. Bono, E. Del Giudice, and G. Preparata, Int. J. Mod. Phys. B **9**, 1813 (1995); E. Del Giudice and G. Preparata, "A new QED picture of water", in Macroscopic Quantum Coherence, eds. E. Sassaroli, Y. N. Srivastava, J. Swain and A. Widom (World Scientific, Singapore 1998); E. Del Giudice, Journal of Physics: Conference Series **67**, 012006 (2007); M. Buzzacchi, E. Del Giudice, and G. Preparata, Int. J. Mod. Phys. B **16**, 3771 (2002); E. Del Giudice, A.

Galimberti, L. Gamberale, and G. Preparata, Mod. Phys. Lett. B **9**, 953 (1995); E. Del Giudice, M. Fleischmann, G. Preparata, and G. Talpo, Bioelectromagnetics, **23**, 522 (2002); E. Del Giudice, G. Preparata, and M. Fleischmann, J. Elec. Chem. **482**, 110 (2000).

[33] S. Sivasubramanian, A. Widom, and Y.N. Srivastava, Physica A **301**, 241 (2001); Int. J. Mod. Phys. B **15**, 537 (2001); Mod. Phys. Lett. B **16**, 1201 (2002); J. Phys. Condens. Matter **15**, 1109 (2003); C. Emary and T. Brandes, Phys. Rev. E **67**, 066203 (2003); M. Apostol, Phys. Lett. A **373**, 379 (2009).

[34] C. A. Yinnon and T. A. Yinnon, Mod. Phys. Lett. B **23**, 1959 (2009).

[35] C. Huang, et al., Proc. Natl. Acad. Sci. USA **106**, 15214 (2009).

[36] J. M. Zheng, W. C. Chin, E. Khijniak, E. Khijniak Jr., and G. H. Pollack, Adv. Coll. Inter. Sci. **23**, 19 (2006); G. H. Pollack, Int. J. Des. Nat. Ecodyn. **5**, 27 (2010); B. Chai, H. Yoo, and G. H. Pollack, J. Phys. Chem. B **113**, 13953 (2009); B. Chai and G. H. Pollack, J. Phys. Chem. B **114**, 5371 (2010); B. Chai, J. M. Zheng, Q. Zhao, and G. H. Pollack, J. Phys. Chem. A **112**, 2242 (2008); B. Chai and G. H. Pollack, J. Phys. Chem. B **114**, 5371 (2010); G. H. Pollack, The Fourth Phase of Water – Beyond Solid, Liquid, and Vapor (Ebner and Sons Publishers Seattle, USA, 2013).

[37] T. A. Yinnon, V. Elia, E. Napoli, and Z.-Q. Liu, Supramolecular ordering of water induced by interfaces: an experimental and theoretical study, to be submitted.

[38] E. C. Fuchs, P. Baroni, B. Bitschnau, and L. Noirez, J. Phys. D **43**, 105502 (2010).

[39] E. Del Giudice, E. C. Fuchs, and G. Vitiello, Water **2**, 69 (2010).

[40] C. L. M. H. Navier, Mem. Acad. R. Sci. Inst. France **6**, 839 (1827).

[41] C. Neto, D. R. Evans, E. Bonaccurso, H.-J. Butt, and V. S. J. Craig, Rep. Prog. Phys. **68**, 2859 (2005).

[42] S. K. Ranjith, B. S. V. Patnaik, and S. Vedantam, Phys. Rev. E **87**, 033303 (2013).

[43] F.-Q. Song and L. Yu, Chinese Journal of Hydrodynamics A **28**, 128 (2013).

[44] J. Mathews and R. L. Walker, Mathematical Methods of Physics (2nd ed.) (Addison-Wesley, New York 1971).

[45] J.-L. Xu and Y.-X Li, International Journal of Heat and Mass Transfer **50**, 2571 (2007).

[46] O. I. Vinogradova and A. V. Belyaev, Journal of Physics: Condensed Matter **23**, 184104 (2011).

[47] J.-H. J. Cho, B. M. Law, and F. Rieutord, Phys. Rev. Lett. **92**, 166102 (2004).

Figure Captions

Fig. 1: (Color online) Schematic picture of the PLFM operated with DC fields. The device consists of a two dimensional frame with two graphite (or copper) electrodes (gray strips) on the sides for electrolysis of the liquid film (blue-green zone). The radius and diameter of the film are denoted, respectively, as R and D. The frame is made of an ordinary blank printed circuit board with a circular (or square) hole at the center. The diameter of the hole may vary from several centimeters to less than a millimeter. Suspended liquid films as thin as hundreds of nanometers or less may be created by brushing the liquid on the frame. The electric current $\boldsymbol{J}_{el}$ (induced by electrolysis field $\boldsymbol{E}_{el}$) and an external electric field $\boldsymbol{E}_{ext}$ are produced by two circuits with voltage U_{el} and U_{ext}, respectively. $\boldsymbol{E}_{ext}$, induced by two plates (striate strips) of a large capacitor, is perpendicular to $\boldsymbol{J}_{el}$. When the magnitudes of $\boldsymbol{E}_{el}$ and $\boldsymbol{E}_{ext}$ are above threshold values, the film rotates, i.e., constitutes a motor. The rotation direction obeys a right-hand rule, i.e., $\boldsymbol{E}_{ext} \times \boldsymbol{J}_{el}$. If the DC electric sources (bold vertical lines in circuits) are replace by AC ones, PLFM can also rotate in AC fields with the same frequencies.

Fig. 2: (Color online) Schematic transverse cross-sections of an infinite long cylindrical channel filled with liquid, with slip boundary conditions described by different slip lengths l_s. R_c denotes the channel's radius. (a) For $-R_c < l_s < 0$, the liquid's linear velocity in the channel, i.e., $u_c(r,t)$ (represented with orange arrows) as a function of r quickly diminishes to zero in the liquid near the boundary if there is negative slip at the liquid-solid interface. Pink dotted arrows denote an imaginary reverse flow. (b) For $l_s = 0$, $u_c(r,t)$ gradually diminishes to zero near the boundary if there is no slip at the solid-liquid interface, i.e., $u_s = 0$. (c) For $0 < l_s < \infty$, when boundary slip occurs at the solid-liquid interface, there is relative velocity between fluid flow and the cylinder boundary, i.e., $u_s > 0$. (d) For $l_s = \infty$, the solid-liquid interface does not exert any resistance on the fluid, i.e., $u_c(r,t)$ is independent of r and $u_s = u_c(r,t)$. The horizontal dash-dot lines and the horizontal dotted lines represent the central line of channels and the no-slip surfaces, respectively.

Fig. 3: (Color online) Schematic linear velocity's profiles of the slip boundary conditions, with different slip lengths l_s in a rotating liquid film. (a) $-R < l_s < 0$, negative-slip boundary; (b) $l_s = 0$, no-slip boundary; (c) $0 < l_s < \infty$, partial-slip boundary; (d) $l_s = \infty$, perfect-slip boundary.

Fig. 4: (Color online) The profiles of the angular velocity of the DCM with four different boundary conditions represented by different values of k at different times: (a) $k = -0.1$; (b) $k = 10^{-3}$; (c) $k = 1$; (d) $k = 10^{3}$. The insets show the profiles of the corresponding linear velocity of each figure.

Fig. 5: (Color online) The profiles of the angular velocity of the steady rotating DCM and ACM with different k values. k varies from -0.1 to 10^{3}. (a) DCM; (b) ACM with $f = 50$Hz and $\varphi = 0$; (c) ACM with $f = 0.5$Hz and $\varphi = 0$; (d) ACM with $f = 0.5$Hz and $\varphi = 5\pi/12$. The insets show the profiles of the corresponding linear velocity of each figure. Obviously, the rotation properties of the DCM depend on k, while those of the ACM are associated with k as well as these depend on the frequencies and on the phase difference of the AC fields.

Fig. 6: (Color online) The profiles of the angular velocity of the steady rotating ACM with different values of f for $\varphi = 0$ at time $t = 1000$s. f varies from 0.05 Hz to 500Hz. (a) $k = -0.1$; (b) $k = 10^{-3}$; (c) $k = 1$; (d) $k = 10^{3}$. The insets show the profiles of the corresponding linear velocity of each figure. Obviously, the rotation properties around the film's center depend on f, while those near the film's boundary are associated with k. As f decreases, the angular velocities vary from a monotonically decreasing function to a first increasing then decreasing function. As k increases, the ACM subsequently exhibits negative-slip, no-slip, partial-slip, perfect-slip behaviors.

Fig. 7: (Color online) The profiles of the angular velocity of the rotating ACM with different k values for various values of φ ($\varphi = 0$, $\pi/6$, $\pi/4$, $\pi/3$, $5\pi/12$) at time $t = 1000$s: (a) $k = -0.1$; (b) $k = 10^{-3}$; (c) $k = 1$; (d) $k = 10^{3}$. The frequencies of the AC fields are 50Hz. The insets show the profiles of the corresponding linear velocity of each figure. Obviously, the angular velocities are decreasing functions of the radius. On comparing curves in this figure with those with $t = 1000$s in Fig. 4, for the corresponding k values, one finds that the ACM and the DCM exhibit similar characteristics when AC fields' frequencies are large (e.g., $f = 50$Hz). As φ increases, the rotation speed decreases gradually.

Fig. 8: (Color online) The profiles of the angular velocity of the rotating ACM with different k values for various values of φ ($\varphi = 0$, $\pi/6$, $\pi/4$, $\pi/3$, $5\pi/12$) at time $t = 1000$s: (a) $k = -0.1$; (b) $k = 10^{-3}$; (c) $k = 1$; (d) $k = 10^{3}$. The insets show the profiles of the

corresponding linear velocity of each figure. The frequencies of the AC fields are 0.5Hz. As φ increases, the rotation speed not only decreases gradually, but also its maximum moves away from the center of the film.